Fault Tolerant Attitude Estimation Strategy for a Quadrotor UAV under Total Sensor Failure

Boualem Nasri*, Abderrezak Guessoum*, Akram Adnane, Lotfi Mostefai*****

**LSET, Laboratoire des Systèmes Électriques et Télécommande, Faculté de Technologie Université Blida 1, B.P 270, Route de soumaa, Blida, Algérie (e-mail : nasri.boualem@gmail.com; abderguessoum@gmail.com)*
*** Space Mechanics Research Department, Satellite Development Center CDS, BP 4065 Ibn Rochd USTO, Oran, Algeria (e-mail: aadnane@cds.asal.dz)*
**** LGE, Genie Electrotechnics Laboratory, Dr.Tahar Moulay University of Saida, Algéria (e-mail : latyfo@hotmail.com)*

Abstract: In this paper, we propose a conventional extended Kalman filter (CEKF) based new fault-tolerant scheme for the control of quadrotor drones suffering from a total failure of gyroscope sensor. The fault-tolerant conventional extended Kalman filter (FTCEKF) combines two conventional extended Kalman filters under the name CEKF1 and CEKF2 as well as a fault detection algorithm. In the case of nominal operation of the quadrotor, it is possible to obtain a sufficiently good estimation of the desired attitude, position and speed using the first conventional extended Kalman filter (CEKF1). However, in the presence of a total failure of the gyroscope, this filter leads to the collapse of the whole system. To overcome this type of scenarios, a second filter is used as a backup filter (CEKF2), where its role is to ensure a satisfactory attitude estimation using only a magnetometer. To detect a gyroscope sensor failure, a reconfiguration mechanism based on a probabilistic algorithm to make a decision to switch to the backup filter is proposed in this article. The results show that the proposed FTCEKF scheme is approved to be robust against a total gyroscope failure with higher filtering performance.

Keywords: Quadrotor UAVs, Total sensor failure, Fault tolerant, Conventional extended Kalman filter, Reconfiguration mechanism, Grey Wolf Optimizer (GWO).

1. INTRODUCTION

Fault detection and diagnosis (FDD) and fault tolerant control (FTC) have become very important scientific research projects for air and space vehicles such as: satellites, civil aircraft, Unmanned Aerial Vehicles (UAVs), and so on (Isermann, 2005; Zhang and Jiang, 2008; Alwi et al., 2011; Goupil, 2011). When subjected to total/partial failures of sensors, actuators, or factory faults (Abbaspour et al., 2020), the whole system can be lead to a collapse. Advanced devices in this area must be designed to eliminate the effects of these fault types.

Drones or UAVs are among the devices that are increasingly used in the military and civil domains with a growing interest for applications such as surveillance and rescue missions in dangerous environments. For this purpose, many algorithms are applied in order to reduce the risk and improve the localization accuracy of those aerial vehicles.

In general, several approaches in the literature related to fault tolerance control systems are widely recognized in many papers. In works of (Maybeck and Stevens, 1990; Rauch, 1995; Zhang and Jiang, 2001), the authors presented a reconfiguration of the design of the control system when there is a presence of faults on the sensors/actuators in order to ensure the dynamic performance and the stability of the system. Examples of application areas are: aviation and interceptor terminal guidance with unknown target maneuvers. Two nonlinear adaptive estimators are designed to isolate and estimate partial sensor bias faults in the gyroscope and accelerometer (Avram et al., 2015). In addition, a sliding mode observer is used to estimate the angles of roll and pitch only with accelerometer. In (Caliskan and Hajiyev, 2015; Caliskan and Hajiyev, 2016), a fault-tolerant control system (FTC) was proposed to overcome sensor/actuator failures for unmanned aerial vehicles (UAV). This technique is based on the Kalman filter (KF) and two-stage Kalman filters (TSKF) to detect and isolate faulty sensors and actuators. A new fault detection (FD) scheme based on a neural network adaptive observer is proposed for UAV to detect sensor and actuator faults as well as an EKF filter to tune learning coefficients with the aim of improving the accuracy and response speed of the Neural Network (NN) observer (Abbaspour et al., 2017).

Furthermore, a comparison between the three filters of Madgwick, Mahony and that of extended Kalman in the orientation estimation of a movement is applied to a magnetic and inertial measurement unit (IMU) embedded on a quadcopter. The results presented show that the Mahony filter offers a better estimation than the other filters (Ludwig and Burnham, 2018). A fault detection and isolation algorithm for the attitude estimation of an unmanned aerial vehicle (UAV) is integrated in a duplex IMU architecture in order to compensate for possible failures on the sensors (magnetometers, accelerometers and gyros) (D'Amato et al., 2018). A nonlinear FDD (Fault Detection and Diagnosis) strategy is proposed for a Helicopter with two degrees of freedom, dealing with the detection, identification, and classification of sensor, actuator and component faults using stochastic state estimation approaches. These approaches include IMM (Interacting Multiple Model)-EKF and IMM (Unscented Kalman Filter)-UKF for multiple fault conditions. The results obtained by the IMM-UKF give better fault detection performance (Raghappriya and Kanthalakshmi, 2020). A new fault-tolerant dynamics of a high-altitude, long-endurance unmanned aerial vehicle is proposed in the presence of a partial/total fault in the accelerometer. This technique is based on the Interactive Multiple Models (IMM) filter (Youn et al., 2020a). In (Youn, 2020), the use of a new Magnetic Fault Tolerant Navigation Filter (MFTNF) aims to guarantee the heading and position of the UAV, where it combines a primary KF using the magnetic field and a main KF to estimate attitude and position states, as well as an attitude and heading reference system (AHRS) without a magnetometer as a secondary backup filter. An AFTC (Active fault tolerant control) is proposed in the presence of partial faults on the sensors such as the barometer and the gyroscope along the X-axis of the UAV. Three filters are tested (EKF, UKF, CKF) to detect and isolate faults (Patan and Caliskan, 2022).

For the aforementioned articles, which deal with IMU sensor faults, we notice that some of them are based on the gyroscope and accelerometer sensors to estimate the attitude of the UAV. Without doubting their effectiveness for the considered application, these works nevertheless have limitations as described in Table 1.

To overcome these limitations, as shown in Table 1, we propose a new attitude estimation design based on a UAV fault-tolerant system to ensure better drone stability in the case of a gyroscope total failure. In addition to the simplicity of this approach, it nevertheless constitutes a reliable, flexible and low-cost solution that can be realized/implemented in software, which allow us to avoid mostly complicated components redundancy in the hardware architecture.

The main aim of this work is to develop a fault-tolerant control strategy for a quadrotor in case of total failure on the gyroscope. The latter will be designated under the name fault-tolerant conventional extended Kalman filter (FTCEKF), which will be composed of two conventional extended Kalman filters: CEKF1 and CEKF2, and a decision algorithm. For that, we use a CEKF1 estimation algorithm based on gyroscope and magnetometer measurements to estimate the attitude. In the case that the gyroscope fails, a probabilistic fault detection algorithm switches to the CEKF2 optimized fault-tolerant filter. This filter proves its reliability when only magnetometer measurements are used for attitude estimation. Three sliding mode controllers are applied to the quadrotor, the first to control the attitude, the second for the altitude and the third to control the translational position.

The rest of the article is organized as follows: Section 2 presents the nonlinear model and the quadrotor control laws. The different steps for the design of the fault-tolerant extended Kalman filter are discussed in section 3. The numerical simulation of the two filters CEKF1 and CEKF2 performances are done in section 4. Finally, the conclusion and future work are discussed in Section 5.

2. UAV DYNAMICS AND CONTROL

In this section, a description of the dynamic model equation is presented. Next, the attitude, altitude and position controllers are exposed.

2.1 Quadrotor dynamics model

The quadrotor is a highly coupled under- actuated system with four propellers denoted by $M1, \ldots, M4$, generating the lift forces $F_1, \ldots, F_4$. By considering the earth fixed frame $E(O_E, X, Y, Z)$ and the body fixed frame rigidly attached to the quadrotor $B(O_B, x, y, z)$, the quadrotor model as shown in Fig.1 has six degrees of freedom $(x, y, z, \phi, \theta, \psi) \in \mathbb{R}^6$, where x, y are the coordinates in the horizontal plane and z is the vertical position, ϕ is the roll angle around axis x, θ is the pitch angle around axis y and ψ is the yaw angle around axis z.

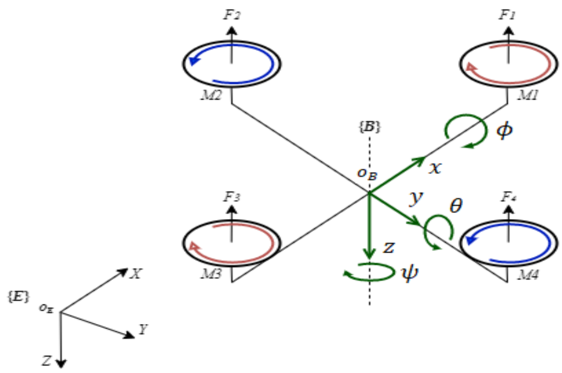

Fig. 1. Quadrotor configuration.

Table 1. Summary of state estimation methods related to sensors fault.

References	Approaches	Limitations
(Avram et al., 2015 ; D'Amato et al., 2018) (Caliskan and Hajiyev, 2015 & 2016)	Model-based/ Adaptive UKF /EKF. Model-based/ KF / Adaptive two-stage KF.	Relies on partial faults of the gyroscope and accelerometer: this does not reflect the case of a total sensors fault.
(Abbaspour et al., 2017)	NN/EKF.	High computational complexity: Need huge historical system performance data.
(Youn, 2020)	Model-based/KF.	The states of the angular position of roll and pitch are not taken into account.
(Patan and Caliskan, 2022)	Model-based/ EKF / UKF/ CKF.	Presence of a partial fault on the gyroscope sensor (the X-axis); position and velocity states are not considered.

In order to model the quadrotor UAV, the following assumptions were made.

Assumption 1: The quadrotor is a rigid and symmetrical body. The propellers are also rigid.

Assumption 2: The lift and drag of each engine are proportional to the square of the propeller velocity.

Assumption 3: The center of mass of the quadrotor and the origin of the frame coincide.

The nonlinear dynamic model of the quadrotor UAV can be described by the following system of differential equations (Bouadi et al., 2011).

$$\begin{cases} \ddot{\phi} = a_1\dot{\psi}\dot{\theta} + a_2\dot{\phi}^2 + a_3\overline{\Omega}\dot{\theta} + b_1u_2 \\ \ddot{\theta} = a_4\dot{\psi}\dot{\phi} + a_5\dot{\theta}^2 + a_6\overline{\Omega}\dot{\phi} + b_2u_3 \\ \ddot{\psi} = a_7\dot{\phi}\dot{\theta} + a_8\dot{\psi}^2 + b_3\,u_4 \end{cases} \quad (1)$$

$$\begin{cases} \ddot{x} = a_9\dot{x} + (u_xu_1)/m \\ \ddot{y} = a_{10}\dot{y} + (u_yu_1)/m \\ \ddot{z} = a_{11}\dot{z} + (c\phi c\theta)u_1/m - \mathrm{g} \end{cases} \quad (2)$$

with

$$\begin{cases} a_1 = \frac{I_x - I_y}{I_z}, a_2 = \frac{-K_{fax}}{I_x}, a_3 = \frac{-J_r}{I_x} \\ a_4 = \frac{I_z - I_x}{I_y}, a_5 = \frac{-K_{fay}}{I_y}, a_6 = \frac{J_r}{I_y} \\ a_7 = \frac{I_x - I_y}{I_z}, a_8 = \frac{-K_{faz}}{I_z}, a_9 = \frac{-K_{fdx}}{m} \\ a_{10} = \frac{-K_{fdy}}{m}, a_{11} = \frac{-K_{fdz}}{m} \\ b_1 = \frac{d}{I_x}, b_2 = \frac{d}{I_y}, b_3 = \frac{C_D}{I_z} \\ \overline{\Omega} = \omega_1 - \omega_2 + \omega_3 - \omega_4 \end{cases} \quad (3)$$

and

$$\begin{cases} u_x = c\phi s\theta c\psi + s\phi s\psi \\ u_y = c\phi s\theta s\psi - s\phi c\psi \end{cases} \quad (4)$$

where $c\phi \equiv cos\phi$ and $s\phi \equiv sin\phi$, (same for $c\theta$, $s\theta$ $c\psi$, $s\psi$), m is the mass of the quadrotor, g is the magnitude of the acceleration of gravity, I_x, I_y and I_z are the inertia elements of the quadrotor for x-axis, y-axis and z-axis, respectively, K_{fax}, K_{fay} and K_{faz} are the aerodynamic coefficients of friction, K_{fdx}, K_{fdy} and K_{fdz} are the positive translational drag coefficients, J_r is actuator's moment inertia, d is the distance between the center of gravity of the quadrotor and propellers rotation axis, $\omega_1, \omega_2, \omega_3$ and ω_4 the angular velocities of the rotors, C_D is the drag coefficient and u_1 represents the total lift force on the body in the z-axis; u_2, u_3 and u_4 are the roll, pitch and yawing torques, respectively.

2.2 Nonlinear control design

A set of sliding mode controllers are proposed to govern the dynamics of the quadrotor. The sliding mode control strategy adopted hereby is similar to the work proposed by (Bouadi et al., 2007).

Let $\underline{X} = \left[\phi, \theta, \psi, \dot{\phi}, \dot{\theta}, \dot{\psi}, x, y, z, \dot{x}, \dot{y}, \dot{z}\ \right]^T$ be the state vector, $\underline{U} = [u_1, u_2, u_3, u_4]^T$ is the control input vector and $\underline{Y} = [x, y, z, \phi, \theta, \psi]^T$ is the output vector. The block diagram of the proposed control system is given in Fig. 2. First, the position controller generates the virtual control vector $[u_{vx}, u_{vy}]$ for the (x, y) positions control. Then, three attitude controllers are used to generate the control inputs u_2, u_3 and u_4 for the roll, pitch, and yaw angles $[\phi, \theta, \psi]^T$ respectively, based on the desired attitude trajectory $[\phi_d, \theta_d, \psi_d]^T$. Note that the nonholonomic constraints block use the virtual control vector and the desired yaw angle ψ_d to generate the desired roll and pitch angles ϕ_d, θ_d. Finally, an altitude controller is used to generate the control input u_1 for the vertical movement (z).

- Nonholonomic constraints

From the Equation (4) we can extract the expressions the nonholonomic constraints which represent the relations between the two angles ϕ and θ and the components of the acceleration.

$$\begin{cases} \phi = \arcsin(u_x s\psi - u_y c\psi) \\ \theta = \arcsin\left(\left(u_x c\psi + u_y s\psi\right) / c\phi\right) \end{cases} \quad (5)$$

Consequently, Equation (5) can be used to formulate the nonholonomic constraints of the desired angles ϕ_d and θ_d as follows

$$\begin{cases} \phi_d = \arcsin(u_{vx} s\psi_d - u_{vy} c\psi_d) \\ \theta_d = \arcsin\left(\left(u_{vx} c\psi_d + u_{vy} s\psi_d\right) / c\phi_d\right) \end{cases} \quad (6)$$

2.2.1 *The control Strategy*

The conventional way to design a sliding mode control law amounts, at first, to choosing the sliding surface which ensures the convergence of the state dynamics of the system towards the desired equilibrium state. The first order switching functions is selected as

$$s = \dot{e} + \lambda e \quad (7)$$

where λ is positive constant coefficient and $e = Y_d - Y$ such that Y_d being the reference value of variable Y.

To obtain the sliding mode regime, the switching function derivative should be chosen as (Hung et al., 1993)

$$\dot{s} = -k\ sign(s) \quad (8)$$

such as

$$sign(s) = \begin{cases} \frac{s}{|s|} &, \text{ for } s \neq 0 \\ 0 &, \text{ for } s = 0 \end{cases} \quad (9)$$

where k is a positive gain affecting the conversion speed of the discontinuous control and $sign$ is the sign function.

- Sliding mode controller design for (ϕ)

Consider the first rotational subsystem expressed in Equation (1)

$$\ddot{\phi} = a_1\dot{\psi}\dot{\theta} + a_2\dot{\phi}^2 + a_3\overline{\Omega}\dot{\theta} + b_1u_2 \quad (10)$$

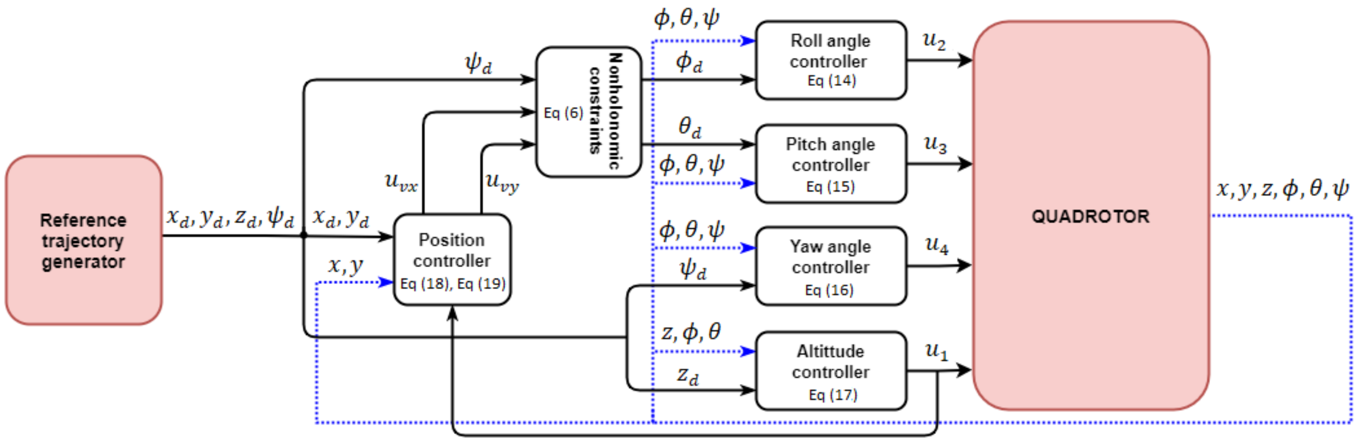

Fig. 2. Synoptic scheme of the proposed control system.

Using Equation (7), the roll angle's switching function is given as

$$s_\phi = \dot\phi_d - \dot\phi + \lambda_\phi(\phi_d - \phi) \tag{11}$$

By taking the time derivative of Equation (11), we can obtain

$$\dot s_\phi = \ddot\phi_d - \ddot\phi + \lambda_\phi(\dot\phi_d - \dot\phi) \tag{12}$$

According to Equation (8), we impose

$$\dot s_\phi = -k_\phi sign(s_\phi) \tag{13}$$

Thus, by substituting Equation (10) into the equality between Equation (12) and Equation (13), the control law u_2 of the roll angle can be deduced.

$$u_2 = \frac{1}{b_1}\left(k_\phi sign(s_\phi) - a_1\dot\theta\dot\psi - a_2\dot\phi^2 - a_3\bar\Omega\dot\theta + \ddot\phi_d + \lambda_\phi(\dot\phi_d - \dot\phi)\right) \tag{14}$$

The same steps are followed to extract other control laws.

- Results of sliding mode controllers for (θ, ψ, x, y, z) are given as

$$u_3 = \frac{1}{b_2}\left(k_\theta sign(s_\theta) - a_4\dot\phi\dot\psi - a_5\dot\theta^2 + a_6\bar\Omega\dot\phi\right) + \ddot\theta_d + \lambda_\theta(\dot\theta_d - \dot\theta)) \tag{15}$$

$$u_4 = \frac{1}{b_4}\left(k_\psi sign(s_\psi) - a_7\dot\phi\dot\theta - a_8\dot\psi^2\right) + \ddot\psi_d + \lambda_\psi(\dot\psi_d - \dot\psi)) \tag{16}$$

$$u_1 = \frac{m}{c\phi c\theta}\left(k_z sign(s_z) - a_{11}\dot z + \ddot z_d + \lambda_z(\dot z_d - \dot z) + g\right) \tag{17}$$

$$u_{vx} = \frac{m}{u_1}\left(k_x sign(s_x) - a_9\dot x + \ddot x_d + \lambda_x(\dot x_d - \dot x)\right) \tag{18}$$

$$u_1 \neq 0$$

$$u_{vy} = \frac{m}{u_1}\left(k_y sign(s_y) - a_{10}\dot y + \ddot y_d + \lambda_y(\dot y_d - \dot y)\right) \tag{19}$$

$$u_1 \neq 0$$

where $\{k_x, \lambda_x, k_y, \lambda_y, k_z, \lambda_z\}$, $\{k_\phi, \lambda_\phi, k_\theta, \lambda_\theta, k_\psi, \lambda_\psi\}$ are the positive gains of the controllers.

The parameter set of the sliding mode controller are tuned by using a metaheuristic optimization technique. The issue of parameters calculation is developed in subsection 3.3.

2.2.2 *Stability Analysis*

Theorem: The nonlinear quadrotor dynamics described by Equations (1) and (2), under the control law given in Equations (14) to (19) ensures/guarantees that the closed loop controlled system is asymptotically stable in the sense of Lyapunov, i.e. the tracking errors are regulated in the sense that, s_i approaches 0 ($e_i \to 0$ and $\dot e_i \to 0$).

Proof. Selecting the following Lyapunov candidate function

$$V = \frac{1}{2}\sum_{i=\phi}^{z} s_i^2 \quad , \quad i \in \{\phi, \theta, \psi, x, y, z\} \tag{20}$$

Its time derivative is

$$\dot V = \sum_{i=\phi}^{z} s_i \dot s_i \tag{21}$$

With respect to Equation (8), the derivative of V is given as

$$\dot V = \sum_{i=\phi}^{z} s_i(-k_i sign(s_i)) \le \sum_{i=\phi}^{z}(-k_i|s_i|) \tag{22}$$

The obtained Equation (22) implies that $\dot V$ will remain negative. According to the Lyapunov stability theorem, the applied control laws guarantee the asymptotic convergence of the tracking errors to zero for the nonlinear dynamic model of the quadrotor. Therefore, the Theorem has been verified.

Remark 2: The chattering phenomenon is well known to be the main drawback of the sliding mode control approach. In order to reduce the effect of this phenomenon, the sign function can be replaced by saturation function called "sat", the expression of which is as follows (Slotine and Li, 1991)

$$sat\,(s) = \begin{cases} sign(s), & |s| > \sigma \\ \frac{s}{\sigma}, & |s| \le \sigma \end{cases} \tag{23}$$

with σ is the boundary layer thickness.

3. ATTITUDE ESTIMATION AND DESIGN

The states of the quadrotor model can be estimated via an accurate attitude filtering system, which combines the information of the model with the information of the sensors measurements in order to predict the best estimates of states.

3.1 Sensor models

Three sensors are used to estimate the full state of the quadrotor, namely, the magnetometer, the gyroscope and the GPS sensor. The gyroscope provides the angular velocity measurements, while the magnetometer measures the magnetic field strength and the GPS is used to provide quadrotor position and speed measurements.

3.1.1 Magnetometer model

The magnetometer measures geomagnetic data at the point where it is positioned. The measurement of the magnetometer model can be given as follows (Ouyang and Abed-Meraim, 2022)

$$\tilde{M} = R_b[m_x\, m_y\, m_z\,]^T + \gamma_M \tag{24}$$

such as

$$R_b = \begin{bmatrix} c\theta c\psi & s\phi s\theta c\psi - c\phi s\psi & c\phi s\theta c\psi + s\phi s\psi \\ c\theta s\psi & s\phi s\theta s\psi + c\phi s\psi & c\phi s\theta s\psi - s\phi c\psi \\ -s\theta & s\phi c\theta & c\phi c\theta \end{bmatrix} \tag{25}$$

where $\tilde{M} = [\tilde{M}_x, \tilde{M}_y, \tilde{M}_z]^T$ is the measured magnetic field expressed in the body frame, R_b is the transition matrix from the earth fixed frame to the frame linked to the body of the quadrotor, $[m_x, m_y, m_z]^T$ are the magnetic fields expressed in the earth fixed frame and $\gamma_M = [m_{bx}, m_{by}, m_{bz}]^T$ is the Gaussian white noise processes of zero average.

3.1.2 Gyroscope model

The gyroscope sensor measures the instantaneous angular rate of the system body with respect to the earth fixed frame. The model of the gyroscope sensor is considered as following (Adnane et al., 2018).

$$\tilde{G} = [\dot{\phi}, \dot{\theta}, \dot{\psi}]^T + \gamma_G \tag{26}$$

where $\tilde{G}$ is the actual value measured by the gyroscope, γ_G is the zero-mean Gaussian noise of the gyroscope sensor.

3.1.3 GPS model

The GPS receiver is used to give a measure of the position and the speed of the UAV. This sensor can be modeled by the set of equations (27) and (28) as (Youn et al., 2020b).

$$\tilde{\varrho} = [x\, y\, z]^T + \gamma_\varrho \tag{27}$$

$$\tilde{\xi} = [\dot{x}, \dot{y}, \dot{z}]^T + \gamma_\xi \tag{28}$$

where $\tilde{\varrho}$, γ_ϱ $\tilde{\xi}$ and γ_ξ are the actual positions measured by the GPS receiver and the zero-mean Gaussian position noise, the actual velocities measured by the GPS receiver and the zero-mean Gaussian speed noise, respectively.

3.2 Fault tolerant conventional extended Kalman filter

In the presence of a total failure on the gyroscope, the UAV attitude estimation becomes noticeably erroneous. In that case, a FTCEKF based on two modes (CEKF1, CEKF2) and a probabilistic decision algorithm is applied to the controlled system in order to provide the required attitude knowledge missing from the default occurrence. Figure 3 shows a block diagram illustrating the proposed fault detection and estimation system.

In order to simplify the formulas and equations below, it is taken that $\eta = [\phi, \theta, \psi]^T, \omega = [\dot{\phi}, \dot{\theta}, \dot{\psi}]^T, \varrho = [x, y, z]^T$ and $\xi = [\dot{x}, \dot{y}, \dot{z}]^T$.

3.2.1 Filter Design

In this work, the CEKF is adopted, which is based mainly on four steps (Gelb, 1974; Brown and Hwang, 1992).

Let the random process to be evaluated is described as follows

$$X_{k+1} = \Phi_k X_k + w_k \tag{29}$$

where X_k is the state vector and Φ_k is the state transformation matrix and w_k is process noise vector.

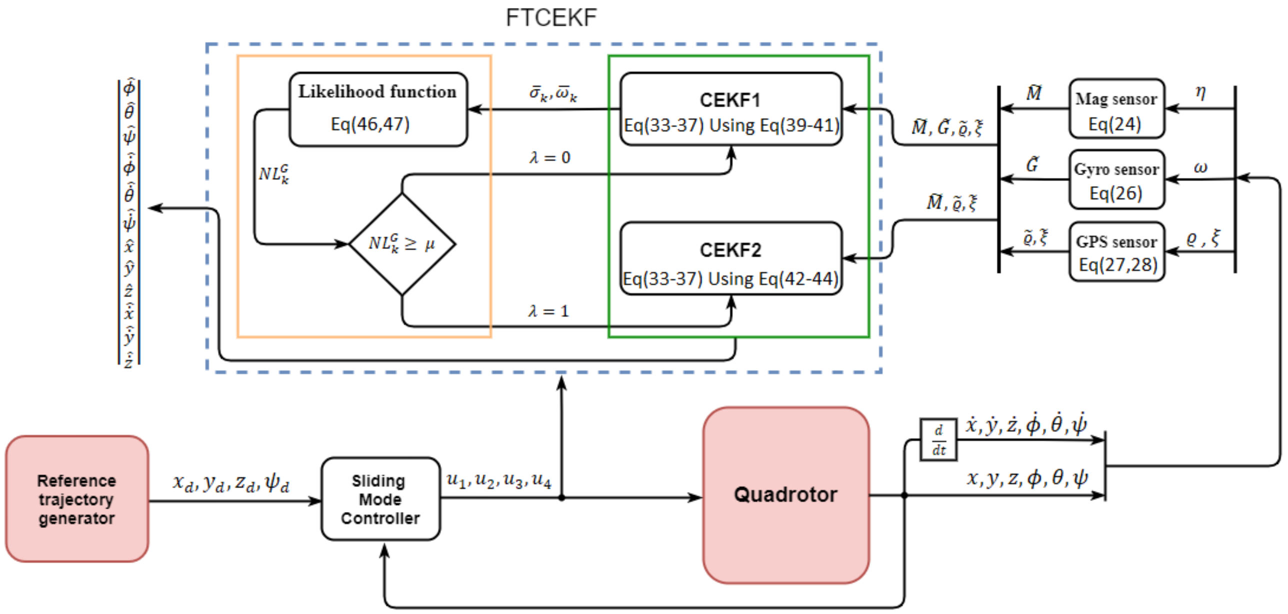

Fig. 3. The structure of the proposed fault detection and estimation system.

The measurement of the process is considered as following

$$Z_k = \mathrm{H}_k X_k + v_k \tag{30}$$

where H_k is the observation matrix and v_k is measurement noise vector.

The state vector to be estimated for the quadrotor is considered as

$$X_k = [\eta_k, \omega_k, \varrho_k, \xi_k]^T \tag{31}$$

Then, the optimal estimates of the filter are defined by

$$\hat{Y}_k = [\hat{\eta}_k, \hat{\omega}_k, \hat{\varrho}_k, \hat{\xi}_k]^T \tag{32}$$

The filter started with initial state vector $\bar{X}_0$ and the initial error covariance matrice $\bar{P}_0$.

<u>Step1: Compute Gain</u>

$$K_k = \bar{P}_k \mathrm{H}_k^T (\mathrm{H}_k \bar{P}_k \mathrm{H}_k^T + R_k)^{-1} \tag{33}$$

where K_k is Kalman gain, $\bar{P}_k$is error covariance of (12×12) dimensions and R_k is the noise covariance matrices.

Noting that each of H_k, Z_k and R_k equations are yet to be defined according to the operating mode of our system.

<u>Step2: Update estimate</u>

$$\hat{X}_k = \bar{X}_k + K_k(Z_k - H_k \bar{X}_k) \tag{34}$$

where $\hat{X}_k$ is the updated state vector, $\bar{X}_k$ is predicted state.

<u>Step3: Update error covariance</u>

$$\hat{P}_k = (I_{12\text{x}12} - K_k H_k)\bar{P}_k \tag{35}$$

where $\hat{P}_k$ is the error covariance matrix of dimension (12×12).

<u>Step4: Project ahead</u>

$$\bar{X}_{k+1} = f(\hat{X}_k, U_k) \tag{36}$$

$$\bar{P}_{k+1} = \Phi_k \hat{P}_k \Phi_k^T + \mathrm{Q}_k \tag{37}$$

such as

$$\Phi_k = I_{12\text{x}12} + \begin{bmatrix} \left.\frac{\partial \dot{\hat{\eta}}_k}{\partial \bar{\eta}_k}\right|_{t=t_k} & \left.\frac{\partial \dot{\hat{\eta}}_k}{\partial \bar{\omega}_k}\right|_{t=t_k} & \left.\frac{\partial \dot{\hat{\eta}}_k}{\partial \bar{\varrho}_k}\right|_{t=t_k} & \left.\frac{\partial \dot{\hat{\eta}}_k}{\partial \bar{\xi}_k}\right|_{t=t_k} \\ \left.\frac{\partial \dot{\hat{\omega}}_k}{\partial \bar{\eta}_k}\right|_{t=t_k} & \left.\frac{\partial \dot{\hat{\omega}}_k}{\partial \bar{\omega}_k}\right|_{t=t_k} & \left.\frac{\partial \dot{\hat{\omega}}_k}{\partial \bar{\varrho}_k}\right|_{t=t_k} & \left.\frac{\partial \dot{\hat{\omega}}_k}{\partial \bar{\xi}_k}\right|_{t=t_k} \\ \left.\frac{\partial \dot{\hat{\varrho}}_k}{\partial \bar{\eta}_k}\right|_{t=t_k} & \left.\frac{\partial \dot{\hat{\varrho}}_k}{\partial \bar{\omega}_k}\right|_{t=t_k} & \left.\frac{\partial \dot{\hat{\varrho}}_k}{\partial \bar{\varrho}_k}\right|_{t=t_k} & \left.\frac{\partial \dot{\hat{\varrho}}_k}{\partial \bar{\xi}_k}\right|_{t=t_k} \\ \left.\frac{\partial \dot{\hat{\xi}}_k}{\partial \bar{\eta}_k}\right|_{t=t_k} & \left.\frac{\partial \dot{\hat{\xi}}_k}{\partial \bar{\omega}_k}\right|_{t=t_k} & \left.\frac{\partial \dot{\hat{\xi}}_k}{\partial \bar{\varrho}_k}\right|_{t=t_k} & \left.\frac{\partial \dot{\hat{\xi}}_k}{\partial \bar{\xi}_k}\right|_{t=t_k} \end{bmatrix} T_s \tag{38}$$

where Q_k is process noise covariance matrix of dimension (12×12), which is calculated by an efficient optimization method, as described in subsection 3.3 and T_s is the sampling period.

- CEKF1 mode

For the first estimator, it is considered that the gyroscope works in a nominal way. Therefore, the terms H_k, R_k and Z_k presented in the CEKF must take the following expressions

$$H_{k_1} = \begin{bmatrix} \frac{\partial \tilde{M}_k}{\partial \bar{\eta}_k} & \frac{\partial \tilde{M}_k}{\partial \bar{\omega}_k} & \frac{\partial \tilde{M}_k}{\partial \bar{\varrho}_k} & \frac{\partial \tilde{M}_k}{\partial \bar{\xi}_k} \\ \frac{\partial \tilde{G}_k}{\partial \bar{\eta}_k} & \frac{\partial \tilde{G}_k}{\partial \bar{\omega}_k} & \frac{\partial \tilde{G}_k}{\partial \bar{\varrho}_k} & \frac{\partial \tilde{G}_k}{\partial \bar{\xi}_k} \\ \frac{\partial \tilde{\varrho}_k}{\partial \bar{\eta}_k} & \frac{\partial \tilde{\varrho}_k}{\partial \bar{\omega}_k} & \frac{\partial \tilde{\varrho}_k}{\partial \bar{\varrho}_k} & \frac{\partial \tilde{\varrho}_k}{\partial \bar{\xi}_k} \\ \frac{\partial \tilde{\xi}_k}{\partial \bar{\eta}_k} & \frac{\partial \tilde{\xi}_k}{\partial \bar{\omega}_k} & \frac{\partial \tilde{\xi}_k}{\partial \bar{\varrho}_k} & \frac{\partial \tilde{\xi}_k}{\partial \bar{\xi}_k} \end{bmatrix} \tag{39}$$

and

$$R_{k_1} = diag\{R_1, R_{2,}, R_3, R_4\} \tag{40}$$

where R_1, R_2, R_3, R_4 are the noise covariance matrices of the magnetometer, gyroscope, GPS position and GPS velocity measurements, respectively.

and

$$Z_{k_1} = [M_k^m \quad G_k^m \quad \varrho_k^m \quad \xi_k^m]^T \tag{41}$$

where M_k^m , G_k^m, ϱ_k^m and ξ_k^m are the sensors' measurements of magnetometer, gyroscope, GPS position and GPS speed, respectively.

- CEKF2 mode

There, we are in the situation where the gyroscope undergoes a breakdown. Hence, the terms H_k, R_k and Z_k becomes

$$H_{k_2} = \begin{bmatrix} \frac{\partial \tilde{M}_k}{\partial \bar{\eta}_k} & \frac{\partial \tilde{M}_k}{\partial \bar{\omega}_k} & \frac{\partial \tilde{M}_k}{\partial \bar{\varrho}_k} & \frac{\partial \tilde{M}_k}{\partial \bar{\xi}_k} \\ \frac{\partial \tilde{\varrho}_k}{\partial \bar{\eta}_k} & \frac{\partial \tilde{\varrho}_k}{\partial \bar{\omega}_k} & \frac{\partial \tilde{\varrho}_k}{\partial \bar{\varrho}_k} & \frac{\partial \tilde{\varrho}_k}{\partial \bar{\xi}_k} \\ \frac{\partial \tilde{\xi}_k}{\partial \bar{\eta}_k} & \frac{\partial \tilde{\xi}_k}{\partial \bar{\omega}_k} & \frac{\partial \tilde{\xi}_k}{\partial \bar{\varrho}_k} & \frac{\partial \tilde{\xi}_k}{\partial \bar{\xi}_k} \end{bmatrix} \tag{42}$$

and

$$R_{k_2} = diag\{R_1, R_3, R_4\} \tag{43}$$

and

$$Z_{k_2} = [M_k^m \quad \varrho_k^m \quad \xi_k^m]^T \tag{44}$$

3.2.2 The probabilistic decision algorithm

The FTCEKF proposed fault tolerant control scheme relies on the detection of the gyroscope sensor failure. It is mainly based on the two modes CEKF1 and CEKF2 coupled with a probabilistic decision algorithm, which manages the switching process that is supposed to occur with the gyroscope dysfunction.

A likelihood function is considered as the designed sensor fault detection device (Lee and Park, 2012). To realize this model, the innovation or residual covariance must be known at each iteration k.

Consider the residual covariance obtained $\bar{\sigma}_k$ from Equation (33) using Equation (39) and Equation (40).

$$\bar{\sigma}_k = H_{k_1} \bar{P}_k H_{k_1}^T + R_{k_1} \tag{45}$$

Thus, the likelihood function can be expressed as

$$L_k^G(\bar{\omega}_k, \bar{\sigma}_k) = \frac{1}{\sqrt{2\pi \|\bar{\sigma}_k\|}} \exp\left\{-\rho \frac{1}{2} \bar{\sigma}_k^{-1} (\bar{\omega}_k)^2\right\} \tag{46}$$

where $\bar{\omega}_k$ is the predicted angular rate obtained by Equation (36) using Equation (39), Equation (40) and Equation (41), ρ

is the scalar penalty used to increase the detection performance.

Here, the Euclidean norm function is applied to the proposed likelihood model in order to calculate the decision rule.

$$NL_k^G = \left\| L_k^G(\bar{\omega}_k, \bar{\sigma}_k) \right\| \quad (47)$$

The decision rule then makes two assumptions

$$\lambda = \begin{cases} 1 & if \quad NL_k^G \geq \mu \\ 0 & if \quad NL_k^G < \mu \end{cases} \quad (48)$$

where μ is the constant threshold characterizing the decision test, λ is the sensor fault indicator.

The output of the decision rule λ is set to 1 when NL_k^G is greater than threshold μ, this implies that an anomaly in the gyroscope is detected. Otherwise, λ is set to 0 when the anomaly is not occurred.

3.3 Design of GWO optimized

To deal with the problem of optimizing the required parameters, the GWO method was chosen. This method is an inspired algorithm from grey wolfs life developed in 2014 by (Mirjalili et al., 2014), imitates the mechanisms of the leadership hierarchy. It models the behaviors of a pack containing four types of gray wolves, three of which are used as leaders α, β, δ and subordinates γ (Fig. 4).

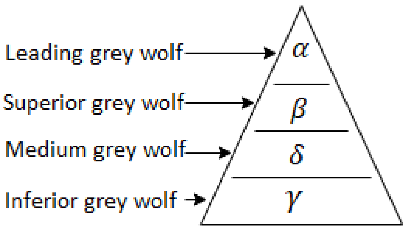

Fig. 4. The hierarchy of the grey wolf pack.

The positions of the wolves α, β and δ are updated taking into account their locations which obtain the best scores. Each wolf calculates its distance from the three optimal solutions by Equations (49) to (52). Then we use Equation (53) to update its position.

$$\begin{cases} \vec{A} = 2\vec{a}\,.\vec{r}_1 - \vec{a} \\ \vec{B} = 2\vec{r}_2 \end{cases} \quad (49)$$

such as

$$\vec{a} = 2 - 2 * n/n\_max \quad (50)$$

where $\vec{A}$ and $\vec{B}$ are two vectors of coefficients, $\vec{r}_1$ and $\vec{r}_2$ are random vectors in the interval $[0,1]$, n is the actual number of iterations and n_max indicates the maximum number of iterations.

$$\begin{cases} \vec{D}_\alpha = |\vec{B}\,.\,\vec{X}_\alpha - \vec{X}| \\ \vec{D}_\beta = |\vec{B}\,.\,\vec{X}_\beta - \vec{X}| \\ \vec{D}_\delta = |\vec{B}\,.\,\vec{X}_\delta - \vec{X}| \end{cases} \quad (51)$$

$$\begin{cases} \vec{X}_1 = \vec{X}_\alpha - \vec{A}\,.\vec{D}_\alpha \\ \vec{X}_2 = \vec{X}_\beta - \vec{A}\,.\vec{D}_\beta \\ \vec{X}_3 = \vec{X}_\delta - \vec{A}\,.\vec{D}_\delta \end{cases} \quad (52)$$

$$\vec{X}(n+1) = \frac{\vec{X}_1 + \vec{X}_2 + \vec{X}_3}{3} \quad (53)$$

where $\vec{X}_\alpha, \vec{X}_\beta$ and $\vec{X}_\delta$ represents the position vectors of the α, β and δ , respectively, $\vec{X}$ indicates the position of the current grey wolf and $\vec{D}_\alpha, \vec{D}_\beta$ and $\vec{D}_\delta$ mean the distance vectors between α, β, and δ, respectively.

In the following section we implemented the GWO algorithm to fit the sliding mode controller parameters, as shown in Table 2, $(\varkappa_{i1} = k_x, \lambda_x, k_y, \lambda_y, k_z, \lambda_z, k_\phi, \lambda_\phi, k_\theta, \lambda_\theta, k_\psi, \lambda_\psi)$ expressed by Equations (14)-(19) on the one hand, as well as the process noise covariance matrix gains $(\varkappa_{i2} = Q_1, Q_2, Q_3, Q_4)$ of the Kalman filter used in Equation (37) on the other, these gains are described in section 4, Table 5.

The cost functions used for the controllers and the filter are as follows

$$min_{\varkappa i} f(\varkappa_i) = \begin{cases} \sum_{k=1}^{samples} e_{i1}(k)^2 \\ \\ \sum_{k=1}^{samples} e_{i2}(k)^2 \end{cases} \quad (54)$$

such as

$$\begin{cases} e_{i1} = e_\phi + e_\theta + e_\psi + e_x + e_y + e_z \\ \\ e_{i2} = \hat{e}_p + \hat{e}_q + \hat{e}_r \end{cases} \quad (55)$$

where the attitude errors and translation errors are represented by $(e_\phi, e_\theta, e_\psi)$ and (e_x, e_y, e_z), respectively. The angular velocity estimation errors are represented by $\hat{e}_p, \hat{e}_q$ and $\hat{e}_r$.

Table 2. Tuning of controller parameters using GWO.

Parameters	GWO
λ_ϕ	89.2344
k_ϕ	49.6759
λ_θ	20.5841
k_θ	99.5799
λ_ψ	8.6804
k_ψ	7.8845
λ_x	1.5213
k_x	5.0000
λ_y	1.5882
k_y	3.4530
λ_z	1.0014
k_z	10.5525

3.3.1 Steps of the optimization algorithm

To obtain the optimized parameters $\varkappa_i$, do the following steps

Step 1: Initialization

– The reference trajectory is randomly chosen.

– Determine the precision value ϵ and the maximal iteration number *Max_iter*.

– Define the number of parameters $\varkappa_i$.

– Select the number of search agent.

– Randomly choose the initial parameters.

Step2: Evaluation of the cost function and choice of the position vectors

– Calculate the cost function using Equation (54).

– Update $\vec{X}_\alpha, \vec{X}_\beta$ and $\vec{X}_\delta$.

Step 3: Update the position of search agents

– Update a, A and B by Equations (49) to (50).

– Calculate the position of each wolf by Equation (52).

– Update the position of the current search by Equation (53).

Step 4: Termination criteria

If $min_{\varkappa i} f(\varkappa_i) < \epsilon$ or *Max_iter* is reached.
– Report the best solution: position of α.
– Exit
Else
– Go to step 2 to perform the next iteration.

4. RESULTS AND DISCUSSIONS

In this section, simulation results are provided to assess the performances of the FTCEKF. The simulation was run under MATLAB/Simulink environment. The total simulation time t_f is 200 sec and the sampling time is fixed at 0.01 sec.

The initial state of the filter estimator is $\bar{X}_0 = [0,0,-pi/3,0,0,0,0,0,0,0,0,0]^T$ and the initial error covariance matrix is $\bar{P}_0 = 0.1 * diag[I_{12X12}]$. Multiple simulations have been carried out involving different trajectories in the literature, among which we used a helical trajectory, which is described in Table 3, having the initial position $(x_0, y_0, z_0) = (0,0,0)$, and a final position $(x_f, y_f, z_f) = (-0.6, -1.9, 60)$.The parameters of the examined UAV are presented in Table 4.

Table 3. Input signals.

State	Reference Trajectory	Time
x	$2\sin(0.3\pi t)$	$[0 - t_f]$
y	$2\cos(0.3\pi t)$	$[0 - t_f]$
z	t	$[0 - t_f]$
ψ	$0.1u_d(t)$	$[0 - t_f]$

In order to evaluate the behavior of the UAV under a total failure of the gyroscope sensor, the simulation of two scenarios is performed. The first case relies on the CEKF1 mode only, while the second considers the use of all components of the FTCEKF as represented inside the dashed line block in the Fig. 3. Table 5 illustrates the obtained results of the two scenarios in terms of the calculated attitude error expressed by the root mean square error (RMSE).

For each scenario we tried to make our simulation as realistic as possible by adding certain constraints such as

- Roll angle $\phi \in [-\pi/2, \pi/2]$.
- Pitch angle $\theta \in [-\pi/2, \pi/2]$.
- Yaw angle $\psi \in [-\pi, \pi]$.
- Introduction of noise in the response of the sensors.
- Introduction of a fault at the level of the gyroscope.

Table 4. Quadrotor general parameters.

Specification	Parameter	Value
Quadrotor mass	$m\ (Kg)$	0.486
inertia on x axis	$I_x(N.m/rad/s^2)$	$3.8278e^{-3}$
inertia on y axis	$I_y(N.m/rad/s^2)$	$3.8278e^{-3}$
inertia on z axis	$I_z(N.m/rad/s^2)$	$7.6566e^{-3}$
gravity	g (ms^{-2})	9.8
Distance	$d\ (m)$	0.25
aerodynamic friction torque along x	$K_{fax}\ (N/rad/s)$	$5.5670e^{-4}$
aerodynamic friction torque along y	$K_{fay}\ (N/rad/s)$	$5.5670e^{-4}$
aerodynamic friction torque along z	$K_{faz}\ (N/rad/s)$	$6.3540e^{-4}$
drag force along x	$K_{fdx}\ (N/m/s)$	$5.5670e^{-4}$
drag force along y	$K_{fdy}\ (N/m/s)$	$5.5670e^{-4}$
drag force along z	$K_{fdz}\ (N/m/s)$	$6.3540e^{-4}$
lift force coefficient	$K_p\ (N.m/rad/s)$	$2.9842e^{-5}$
drag force coefficient	$C_D\ (N.m/rad/s)$	$3.2320e^{-7}$
rotor inertia	$J_r\ (N.m/rad/s^2)$	$2.8385.e^{-5}$

4.1 Scenario 1: CEKF1 application case

In this scenario, we are going to test the behavior of CEKF1 mode alone. Figures 5, 6 and 7 illustrate clearly the attitude angles properly estimated with sufficient precision (stabilization after a period of less than 3 sec) during the first 30 sec, where the gyroscope is operating without any faults. The estimation error remains in a range of approximately between -1 and $+1$ deg as seen in Fig. 8. Once the fault occurs in the sensor, the attitude estimation scheme based on CEKF1 shows a gradual degradation in the performances until total divergence.

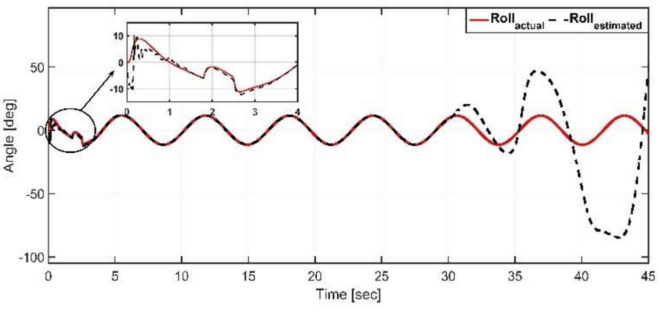

Fig. 5. Roll response of the system using CEKF1 mode.

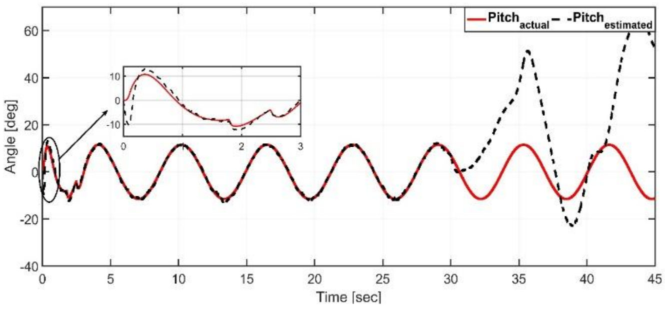

Fig. 6. Pitch response of the system using CEKF1 mode.

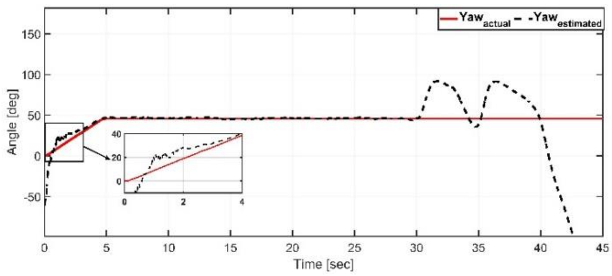

Fig. 7. Yaw response of the system using CEKF1 mode.

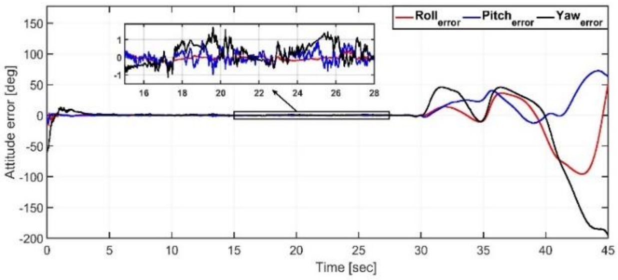

Fig. 8. Quadrotor attitude estimation error using CEKF1 mode.

4.2 Scenario 2: FTCEKF application case

The proposed FTCEKF scheme is evaluated in the second scenario where CEKF1 mode is considered, along with CEKF2 mode and a probabilistic decision strategy. The responses obtained in this scenario are illustrated, demonstrating an improvement in the performances after optimizing the parameters of the process noise covariance matrix gains.

Figure 9-a shows the change in the value of the likelihood function norm at time $t = 30.42\ sec$, taking $\rho = 0.011$, with a small delay of duration $\Delta t = 0.42\ sec$ to detect a total loss of the gyroscope. When NL_k^G is higher than the constant threshold $\mu = 3.08125$, the fault flag will then be declared as shown in Fig.9-b.

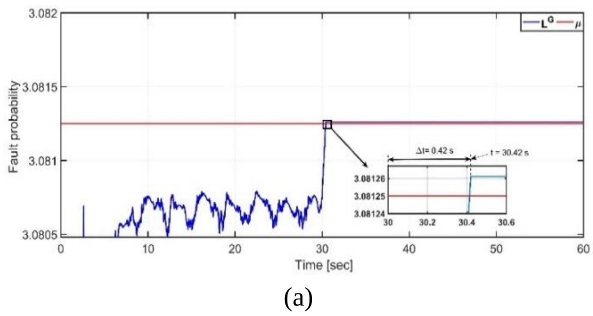

(a)

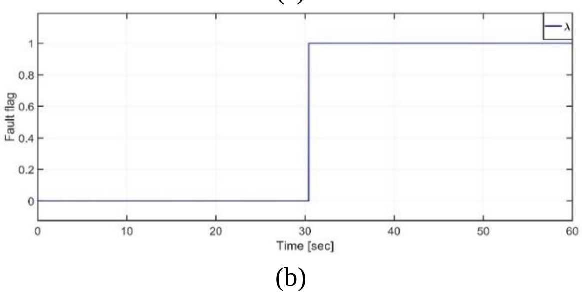

(b)

Fig. 9. Fault detection results: (a) fault probability, (b) fault flag

Figures 10, 11 and 12, respectively, show roll, pitch and yaw estimation responses using FTCEKF. The figures indicate that the proposed estimator is able to handle a total gyroscope sensor failure and follow the real attitude of the UAV. The instant the reconfiguration mechanism detects that the gyroscope has failed, it causes a neglected deviation in the angle responses, so that $RMSE_\phi = 0.31\ deg$ and $RMSE_\theta = 0.7 deg$ over an interval $t \in [30\ ,32]$ and for the yaw $RMSE_\psi = 0.8\ deg$ over an interval $t \in [30\ ,45]\ sec$. We notice that the attitude estimation has remained stable in comparison with the scenario 1.

Figure 13 shows the estimation errors on the three attitude axes of the quadrotor. It is clear through this figure that the estimation error is approximately between $+1$ and $-0.5\ deg$ during the first 30 sec. Then, the error has been slightly increased around $+1.5$ and $-0.5\ deg$.

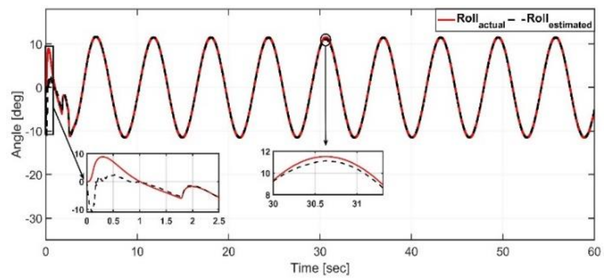

Fig. 10. Roll response of the system using FTCEKF.

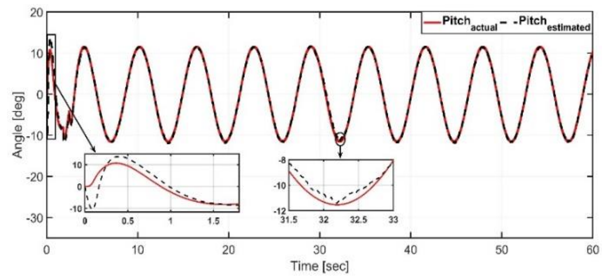

Fig. 11. Pitch response of the system using FTCEKF.

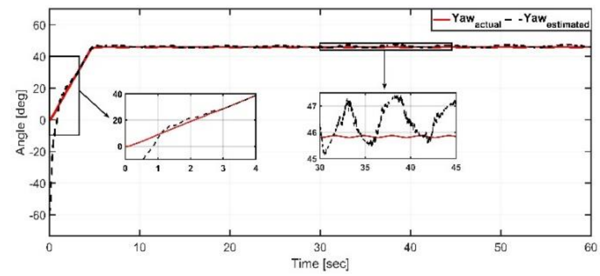

Fig. 12. Yaw response of the system using FTCEKF.

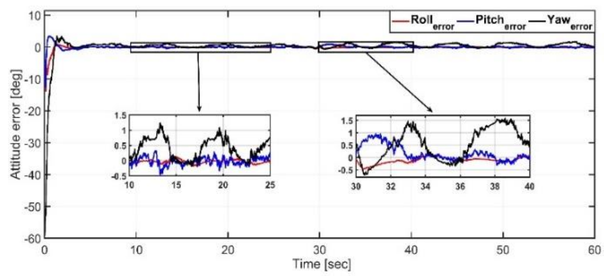

Fig. 13. Quadrotor attitude estimation error using FTCEKF

Figure 14 illustrates how the different angular velocities estimated by the CEKF2 filter progress and show that the stability has not been greatly affected. Figure 15 displays the trajectory response from the moment of detection of the failure by the NL_k^G function, which starts at the position $(\hat{x}_L, \hat{y}_L, \hat{z}_L) = (-1.68, 1.08, 30.43)$ and ends at the final position of the filter $(\hat{x}_f, \hat{y}_f, \hat{z}_f) = (-0.59, -1.91, 59.9)$. The figure shows that the proposed fault tolerance mechanism is done quickly without trajectory deviation.

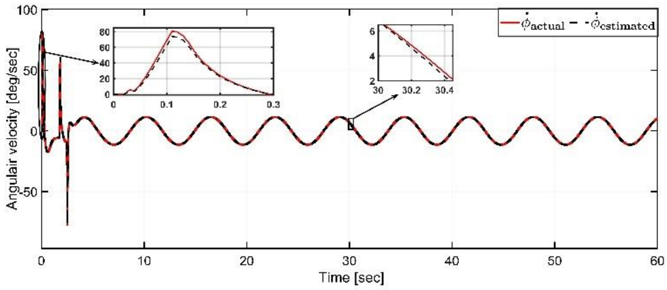

(a)

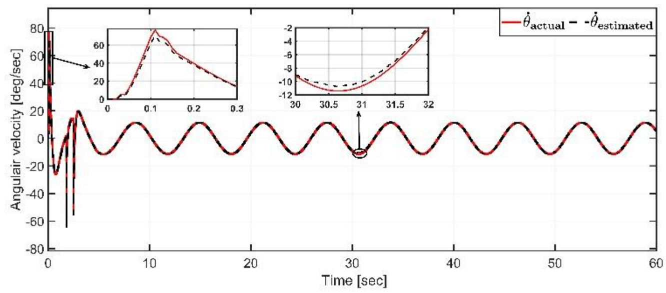

(b)

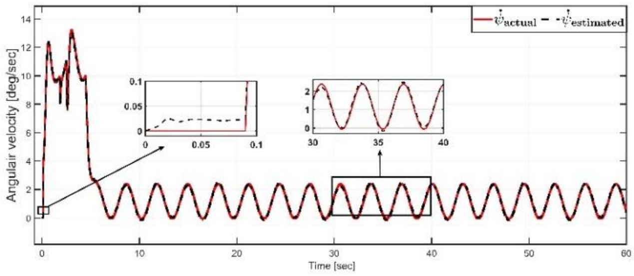

(c)

Fig. 14. Response of the system using FTCEKF: (a) Angular velocity $\dot{\phi}$, (b) Angular velocity $\dot{\theta}$, (c) Angular velocity $\dot{\psi}$

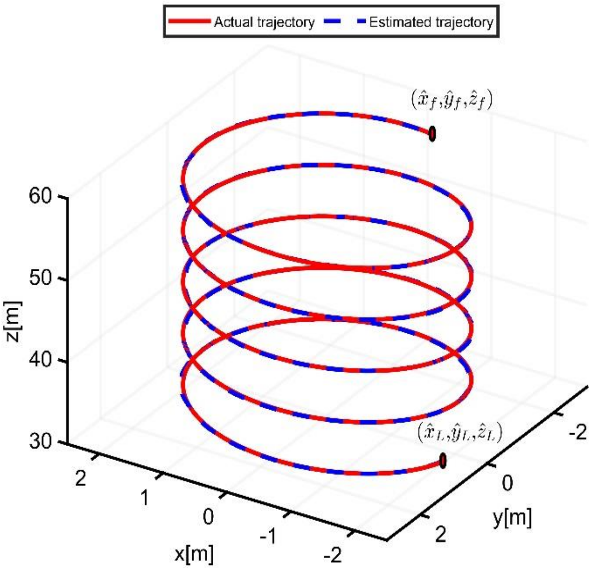

Fig. 15. Trajectory response of the system using FTCEKF.

Table 5. Attitude estimation performance.

Scenario	Gyroscope	Optimization	$RMSE_\phi$ (deg)	$RMSE_\theta$ (deg)	$RMSE_\psi$ (deg)	Magnitude of Error (deg)	R_i	Q_i
Scenario 1	No failure $t \in [0,30]$	Not optimized	0.161	0.387	0.740	0.8509	$R_1 = 0.3 \cdot I_{3\times3}$ $R_2 = 0.05 \cdot I_{3\times3}$ $R_3 = 0.1 \cdot I_{3\times3}$ $R_4 = 0.1 \cdot I_{3\times3}$	$Q_1 = 7.61 \cdot 10^{-11} I_{3\times3}$ $Q_2 = 6.72 \cdot 10^{-7} I_{3\times3}$ $Q_3 = 2.44 \cdot 10^{-8} I_{3\times3}$ $Q_4 = 2.70 \cdot 10^{-10} I_{3\times3}$
	With Failure $t \in]30,45]$	Not optimized	18.803	20.425	30.833	41.483		
Scenario 2	With Failure $t \in]30,60]$	Not optimized	0.173	0.291	1.167	1.215	$R_1 = 0.3 \cdot I_{3\times3}$ $R_3 = 0.1 \cdot I_{3\times3}$ $R_4 = 0.1 \cdot I_{3\times3}$	$Q_1 = 7.61 \cdot 10^{-11} I_{3\times3}$ $Q_2 = 6.72 \cdot 10^{-7} I_{3\times3}$ $Q_3 = 2.44 \cdot 10^{-8} I_{3\times3}$ $Q_4 = 2.70 \cdot 10^{-10} I_{3\times3}$
		Optimized	0.119	0.241	0.839	0.881		$Q_1 = 9.39 \cdot 10^{-7} I_{3\times3}$ $Q_2 = 1.00 \cdot 10^{-7} I_{3\times3}$ $Q_3 = 2.78 \cdot 10^{-6} I_{3\times3}$ $Q_4 = 8.36 \cdot 10^{-5} I_{3\times3}$

5. CONCLUSION

In this paper, two extended Kalman filter based attitude estimation algorithms are developed with the introduction of total gyroscope failure to ensure high and reliable accuracy estimation of the UAV attitude. The results of the simulations show that the CEKF2 algorithm is highly reliable in accurately estimating the attitude and this is due to the quality of faults tolerance. On the other hand, in the nominal case the CEKF1 gives a stable attitude estimate, nevertheless it diverges when a failure of the gyroscope is introduced. Moreover, the fault tolerance mechanism based on the probabilistic function gives complete satisfaction when it is necessary to switch from CEKF1 to CEKF2. The CEKF2 algorithm can also be used as an alternative solution to secure the UAV mission. In future work, we plan to carry out experimental tests in order to validate the results obtained on a real quadrotor.

REFERENCES

Abbaspour A., Aboutalebi P., Yen K.K. and Sargolzaei A. (2017). Neural adaptive observer-based sensor and actuator fault detection in nonlinear systems: Application in UAV. *ISA transactions,* 67**,** 317-329.

Abbaspour A., Mokhtari S., Sargolzaei A. and Yen K.K. (2020). A survey on active fault-tolerant control systems. *Electronics,* 9**,** 1513.

Adnane A., Jiang H., Mohammed M.A.S., Bellar A. and Foitih Z.A. (2018). Reliable Kalman filtering for satellite attitude estimation under gyroscope partial failure. 2018 2nd IEEE Advanced Information Management, Communicates, Electronic and Automation Control Conference (IMCEC). IEEE, 449-454.

Alwi H., Edwards C. and Tan C.P. (2011). *Fault detection and fault-tolerant control using sliding modes,* Springer.

Avram R.C., Zhang X., Campbell J. and Muse J. (2015). IMU sensor fault diagnosis and estimation for quadrotor UAVs. *IFAC-PapersOnLine,* 48**,** 380-385.

Bouadi H., Bouchoucha M. and Tadjine M. (2007). Sliding mode control based on backstepping approach for an UAV type-quadrotor. *World Academy of Science, Engineering and Technology,* 26**,** 22-27.

Bouadi H., Cunha S.S., Drouin A. and Mora-Camino F. (2011). Adaptive sliding mode control for quadrotor attitude stabilization and altitude tracking. 2011 IEEE 12th international symposium on computational intelligence and informatics (CINTI). IEEE, 449-455.

Brown R. and Hwang P. (1992). Introduction to random signals and applied Kalman filtering(Book). *New York, John Wiley & Sons, Inc., 1992. 512*.

Caliskan F. and Hajiyev C. (2015). Reconfigurable control of an UAV against sensor/actuator failures. *IFAC-PapersOnLine,* 48**,** 7-12.

Caliskan F. and Hajiyev C. (2016). Active fault-tolerant control of UAV dynamics against sensor-actuator failures. *Journal of Aerospace Engineering,* 29**,** 04016012.

D'Amato E., Mattei M., Notaro I. and Scordamaglia V. (2018). UAV sensor FDI in duplex attitude estimation architectures using a set-based approach. *IEEE Transactions on Instrumentation and Measurement,* 67**,** 2465-2475.

Gelb A. (1974). *Applied optimal estimation*, MIT press.

Goupil P. (2011). AIRBUS state of the art and practices on FDI and FTC in flight control system. *Control Engineering Practice,* 19**,** 524-539.

Hung J.Y., Gao W. and Hung J.C. (1993). Variable structure control: A survey. *IEEE transactions on industrial electronics,* 40**,** 2-22.

Isermann R. (2005). *Fault-diagnosis systems: an introduction from fault detection to fault tolerance*, Springer Science & Business Media.

Lee J. and Park C.G. (2012). Cascade filter structure for sensor/actuator fault detection and isolation of satellite attitude control system. *International Journal of Control, Automation and Systems,* 10**,** 506-516.

Ludwig S.A. and Burnham K.D. (2018). Comparison of euler estimate using extended Kalman filter, Madgwick and Mahony on quadcopter flight data. 2018 International Conference on Unmanned Aircraft Systems (ICUAS). IEEE, 1236-1241.

Maybeck P.S. and Stevens R.D. (1990). Reconfigurable flight control via multiple model adaptive control methods. 29th IEEE Conference on Decision and Control. IEEE, 3351-3356.

Mirjalili S., Mirjalili S.M. and Lewis A. (2014). Grey wolf optimizer. *Advances in engineering software,* 69**,** 46-61.

Ouyang G. and Abed-Meraim K. (2022). A Survey of Magnetic-Field-Based Indoor Localization. *Electronics,* 11**,** 864.

Patan M.G. and Caliskan F. (2022). Sensor fault–tolerant control of a quadrotor unmanned aerial vehicle. *Proceedings of the Institution of Mechanical Engineers, Part G: Journal of Aerospace Engineering,* 236**,** 417-433.

Raghappriya M. and Kanthalakshmi S. (2020). Non-linear Model-based Stochastic Fault Diagnosis of 2 DoF Helicopter. *Journal of Control Engineering and Applied Informatics,* 22**,** 62-73.

Rauch H.E. (1995). Autonomous control reconfiguration. *IEEE Control Systems Magazine,* 15**,** 37-48.

Slotine J.-J.E. and Li W. (1991). *Applied nonlinear control*, Prentice hall Englewood Cliffs, NJ, 199.

Youn W. (2020). Magnetic Fault–Tolerant Navigation Filter for a UAV. *IEEE Sensors Journal,* 20**,** 13480-13490.

Youn W., Choi H., Cho A., Kim S. and Rhudy M.B. (2020a). Accelerometer fault-tolerant model-aided state estimation for high-altitude long-endurance UAV. *IEEE Transactions on Instrumentation and Measurement,* 69**,** 8539-8553.

Youn W., Choi H.S., Ryu H., Kim S. and Rhudy M.B. (2020b). Model-aided state estimation of HALE UAV with synthetic AOA/SSA for analytical redundancy. *IEEE Sensors Journal,* 20**,** 7929-7940.

Zhang Y. and Jiang J. (2001). Integrated active fault-tolerant control using IMM approach. *IEEE Transactions on Aerospace and Electronic systems,* 37**,** 1221-1235.

Zhang Y. and Jiang J. (2008). Bibliographical review on reconfigurable fault-tolerant control systems. *Annual reviews in control,* 32**,** 229-252.